

# FANSIC: a Fast ANalog SiPM Integrated Circuit for the readout of large silicon photomultipliers

Luca Giangrande<sup>a,\*</sup>, Matthieu Heller<sup>a</sup>, Yannick Favre<sup>a</sup>, Teresa Montaruli<sup>a</sup>

<sup>a</sup>*Département de Physique Nucléaire et Corpusculaire, Faculté de Science, University of Geneva, 24 Quai Ernest-Ansermet, Genève, 1205, Switzerland*

---

## Abstract

Silicon photo-multipliers (SiPM) have been replacing traditional photomultiplier tubes in most light sensing applications. However, when large detection surface coverage is needed, photomultipliers (PMTs) are still the preferred choice. The main reasons are the sensor thermal noise and the duration of the fast component of its signal, both increasing with the sensor surface. In this work we propose an application specific integrated circuit (ASIC), called Fast ANalog SiPM Integrated Circuit (FANSIC), for the readout of large SiPMs addressing these limitations. The ASIC has an active summation stage, which allows to divide a large detection surface into smaller ones offering faster response both in single ended and differential outputs. The high input bandwidth allows to reach full-width-half-maximum (FWHM) signals or the order of 3–5 ns which limits the impact of internal and external uncorrelated noise. The results of the first implementation of FANSIC, designed in CMOS 65 nm technology, is described in this paper.

*Keywords:*

Front-end, ASIC for SiPM, Cherenkov telescope camera

---

## 1. Introduction

FANSIC is a fully analog front-end ASIC with 32 input channels designed to readout and process the signals of large SiPM sensors with single-photon

---

\*Corresponding author

*Email address:* [luca.giangrande@unige.ch](mailto:luca.giangrande@unige.ch) (Luca Giangrande)

*URL:* <https://www.unige.ch/sciences/astroparticle/> (Teresa Montaruli)

resolution, 1 ns peaking time, and dynamic range in hundreds of photo-electrons. The main features of the chip are reported in Table 1. The chip is a prototype intended to confirm the performance achievable on a standard CMOS 65 nm technology node. The aim is to guarantee a short output signal and low noise levels while being compatible with input capacitance values up to 1 nF. This is a key requirement for many applications that handle signals with GHz rate and duration in the nanosecond range. Moreover, processing the signal of large arrays of sensors (bigger than  $6 \times 6 \text{ mm}^2$ ) is a common need for many experiments that require covering large surfaces.

The application target of FANSIC is in cameras of gamma-ray telescopes, like Imaging Atmospheric Cherenkov Telescopes (IACTs) which detect the Cherenkov light produced by atmospheric showers triggered by interaction of atmospheric nuclei with gamma and cosmic rays. This light is produced in flashes with a typical duration shorter than 5-10 ns and most of this signal light is emitted in wavelengths between 320 nm and 550 nm. IACTs employ cameras with hundreds to several thousands of photo-sensors clustered into pixels and located in their focal plane. Most cameras still adopt photomultipliers (PMTs) because their larger size compared to SiPMs allows to cover square-meter surfaces with less complexity and number of components.

Recently, the ETH in Zürich and the University of Geneva have pioneered the adoption of SiPMs in IACTs cameras through the construction and operation of the FACT [1] and SST-1M [2]. The SST-1M camera has 1286 pixels and a linear dimension of about 1 m and is now in operation at the Ondřejov site in Czeck Republic [3]. FANSIC has been designed to be compatible with the requirements of a further evolution to larger dimension cameras with diameters of about 2 m. These Advanced Cameras are intended for the upgrade of the Large-Sized Telescope (LST) of the Cherenkov Telescope Array Observatory (CTAO) [4] during the 30 years of operation foreseen for this new generation of gamma-ray observatory [5].

## 2. Design requirements

This section illustrates the application requirements that drive the design of the analog front-end :

**Sensor.** The proposed upgrade for the LST [5] will feature SiPM instead of PMTs. The upgrade does not consist solely in replacing the 1 inch PMTs

Technology	CMOS 65 nm
Dimensions	12.845 mm <sup>2</sup> (3.584 × 3.584 mm)
Inputs	32 current inputs
Outputs	8 voltage outputs (each sum of four inputs)
Power supply	1.2 V
Power consumption	23 mW (per pixel, i.e. 4 input channels)
Programmable settings	Amplifier bias currents, and buffer AC coupling capacitors
Package	None (bare dies)

Table 1: Main characteristics of the FANSIC chip

with a SiPM array, as it would result in large accumulation of night sky background (NSB) photons. On a typical site as the Los Roque de los Muchachos at La Palma, where CTAO Northern site will be located, the current large size telescope cameras detect 300 MHz per pixel with 1.5-inch PMTs. SiPM sensors are usually built as a collection of individual square-shaped micro-cells with a side in the tens of micro-meters. The adopted size depends on the expected density of photons on the detection plane. Typically, 50  $\mu\text{m}$  or 75  $\mu\text{m}$  micro-cell size SiPMs are used in gamma-ray telescope applications, resulting in several thousands of micro-cells per pixel. The sensor for which FANSIC was designed has been developed in collaboration with Hamamatsu to comply with the requirements of enhanced sensitivity in the near UV spectrum and a faster response.

**Active Summation.** The SiPMs considered for this application are almost twice more sensitive than typically used PMTs, in the wavelengths range from 300 nm to 600 nm [6]. This implies that the pixel size can be reduced while keeping a similar amount of detected photons per pixel. In the proposed camera design, the pixel is hexagonal and its size can be divided by a factor of four which allows to use SiPMs of size of  $\sim 1 \text{ cm}^2$ . This size is larger than that of commonly adopted SiPMs arrays (namely  $3 \times 3$  or  $6 \times 6 \text{ mm}^2$ ) and has an impact on the noise and speed of the sensor. The solution is therefore to split the active area into four distinct channels from which the first requirement on the ASIC design comes from: the ASIC has to feature an active summation stage to cope with noise and speed performance.

The thermal noise contribution of the sensor capacitance can be converted

into an equivalent number of photoelectrons as follows:

$$ENP = \frac{\sqrt{k_b T C_{eq}}}{|e \cdot G|} \quad (1)$$

Where  $k_b$  is the Boltzmann constant,  $T$  is temperature in Kelvin,  $C_{eq}$  is the total capacitance on the output node,  $e$  is the electron charge,  $G$  is the SiPM gain. With the estimated values of  $C_{eq} = 650$  fF,  $G = 104$ ,  $T = 290$ K the equivalent noise corresponds to one photon. Therefore, for the sake of ensuring signal to noise levels compatible with single photon detection, the pixel is sectioned into quarters which are individually readout through dedicated pre-amplifiers. Then the pixel signal is reconstructed by means of an active summation stage in an effort to contain the required load of digitization and data transfer inside the camera.

**Speed.** Depending on the sensor technology and design, the equivalent output capacitance of a of  $1 \text{ cm}^2$  pixel reaches several hundreds pico-Farads and is dominated by the quenching capacitance of the Corsi model. This relatively large sensor capacitance poses several design challenges for the interfacing circuitry. Firstly, the capacitance provides an alternative path for the electrons generated by the SiPM producing an undesired signal attenuation. Secondly, it directly affects the intrinsic fall time of the sensor signal, leading to longer pulses. Thirdly, it introduces an undesirable noise charge contribution, which undermines single-photon detection. The equivalent noise in terms of photo-electrons (ENP) is given by the noise charge associated with the overall output capacitance divided by the charge produced by one photon (see Eq. 1). In order to maintain the required signal-to-noise ratio (SNR) of at least 5, ensuring a very good photon counting capability and allowing to form signal images on top of the NSB, the ASIC speed requirement is derived. To avoid as much as possible the pile-up of NSB photons, a requirement on the FWHM of the amplified signal of 3 ns can limit the contribution of random coincidences. The requirement of the ASIC bandwidth was derived from this specification.

**Dynamic Range.** For the bulk of the events, pixels will receive between 10 and 200 photo-electrons (p.e.) per event. About 1 event over a thousand will have at least one pixel with more than 250 p.e. this condition to derive the requirement on the dynamic range of the ASIC to  $[1, 250]$  p.e. Above

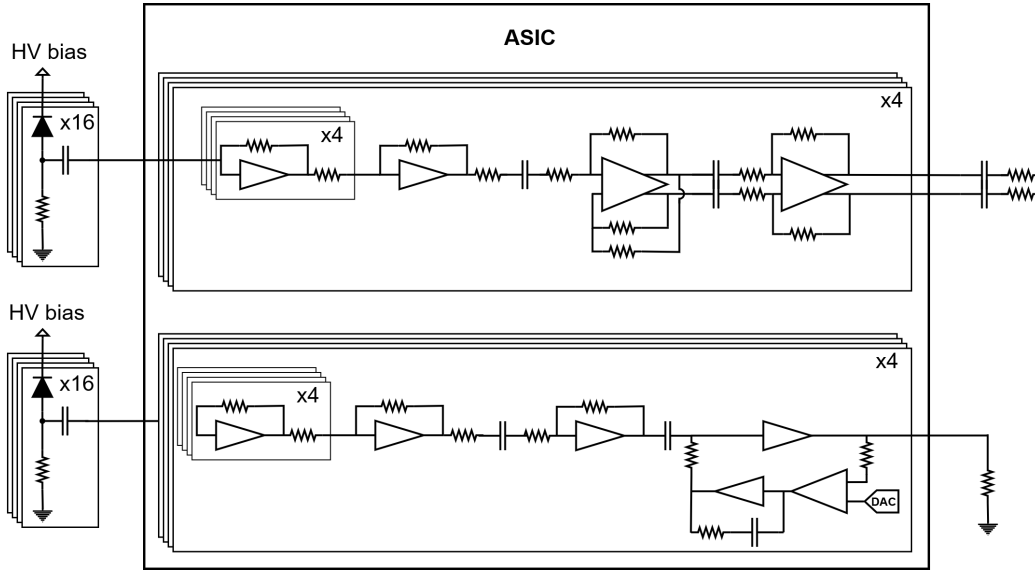


Figure 1: Simplified block diagram of the single ended and differential front-end channels

this range the analogue stage shall saturate, which will entail the linearity while technically extending the dynamic range well further a 1000 p.e. The linearity within the specified dynamic range must be better than 5% after calibration. The front-end performance indicators are expected to comply with the application requirements within such range and are allowed to drop or saturate at higher light intensities. Nonetheless, it is important that the circuit shows a nice saturation behavior in order to recognize out-of-range light intensities.

**Interfaces.** The camera needs to perform a large amount of numerical computation to identify various types of events, therefore the analog output of the front-end needs to be converted to digital through an integrated ADC, either a commercial (such as the ADC12SJ1600 from Texas Instruments) or a custom one. To support both approaches, the ASIC needs to provide its output in both a single-ended and a differential form.

### 3. Front-end design

The main functionalities that a sensor interface needs to provide are: biasing, signal conditioning and buffering. SiPMs are readout from their anode

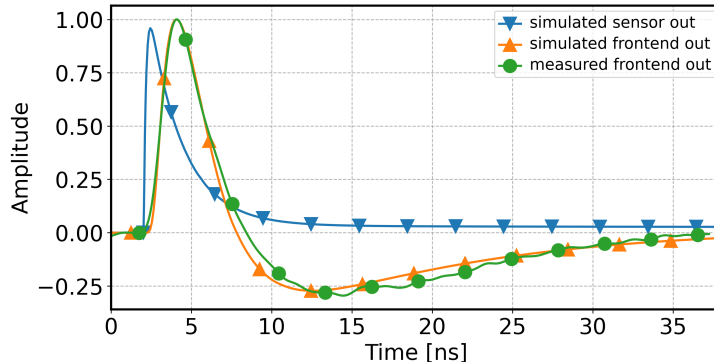


Figure 2: Pulse shapes comparison between the simulated S13360-3075CS-UVE current (blue) and the corresponding front-end output voltage with normalized amplitude both simulated (orange) and the measured (green).

side, which is electrically connected to a low-voltage potential, whereas the anode is connected to a high-voltage source. The low voltage reference point is generated with a resistor to ground which also converts the sensor current pulse into a voltage which is fed to the front-end by means of an AC coupling capacitor. The various front-end stages perform analog signal conditioning through amplification, active summation, filtering and, optionally, pseudo-differential conversion. The purpose of buffering is to preserve the voltage pulse features over the connection with the ADC through PCB traces and cabling ( $50\ \Omega$  characteristic impedance per line). The architecture of the analog front-end is shown in Figure 1, the 8 pixel-channels are grouped by 4 depending on the type of output load they support. For the sake of compatibility with different ADC topologies and to assess the influence of electromagnetic interference within the camera, two types of buffer stages have been designed leading to two signal processing chains which only differ for the topology of their output stage. Both channel types comprise four preamplifiers, a summation stage and an output buffer; the upper channels in the block level representation (Figure 1) can drive a (pseudo) differential AC-coupled  $100\ \Omega$  load, while the lower channels are meant for a single-ended, DC-coupled  $50\ \Omega$  load.

The channels feature adjustable bias currents for the amplifiers and adjustable AC coupling capacitors to accommodate different types of sensors and optimize the output pulse features. Moreover, in case of single ended buffer, it's possible to adjust the output dc offset level (from 20 mV up to

190 mV) for compatibility with DC-level requirements of the ADC.

The S13360-3075CS-UVE output signal is a current pulse with sharp rising time, in the order of hundreds of ps, and two decaying time constants: a faster one around 1 ns and a slower one around 1  $\mu$ s. The effect of the signal conditioning introduced by the sensor interface is shown in Figure 2: the slower time constant is filtered, the pulse duration is slightly increased and an undershoot is introduced. The sensor slow time constant is associated with the quenching of the avalanche carrier multiplication, but it is undesired from the application point of view as its associated exponential decay leads to both an attenuation of the effective gain and a pile-up of the signal tails. The gain attenuation is due to the fact that if a micro-cell is hit during its quenching phase, it can only provide a partial charge in response to a photo-electron. The pile-up is related to the fact that, at pixel-level, all the slow recovering tails add up and introduce a baseline shift proportional to the NSB rate. The degree of gain attenuation depends on the value of the slower time constant, the area of the pixel and the NSB rate. The time evolution of the micro-cell charge follows equation 2:

$$q(t) = q_0 \cdot \left(1 - e^{-\frac{t}{\tau_{\text{slow}}}}\right) \quad (2)$$

where  $q_0$  represents the steady state charge given by the overdrive voltage times the diode capacitance whereas the slow time constant  $\tau_{\text{slow}}$  is given by the product of the quenching resistance and the sum of the diode capacitance plus the quenching capacitance. In order for the micro-cell to be affected by a gain loss smaller than 1% compared to its nominal value, it needs to recharge for a time interval of at least  $4.6 \cdot \tau$ . The hit probability for a given micro-cell (or pixel depending on the hit rate used in the calculation) due to the background can be modeled with a Poisson distribution given in Equation 3:

$$P(n\Delta t) = \frac{(r \cdot \Delta t)^n}{n!} e^{-r \cdot \Delta t} \quad (3)$$

Where  $P(n\Delta t)$  gives the probability of observing  $n$  hits within the time interval  $\Delta t$  and  $r$  is the average hit rate. Hence, the degradation induced on the effective gain can be computed by combining Equation 2 and Equation 3 with  $n = 1$  and integrating the probability density up to the desired number of time constants:

$$G = 1 - \int_0^{\Delta t} e^{-x/\tau} \cdot r \cdot e^{-r \cdot x} dx = 1 + \frac{r}{r + 1/\tau} \left[ e^{-x(r+1/\tau)} \right]_0^{\Delta t} \quad (4)$$

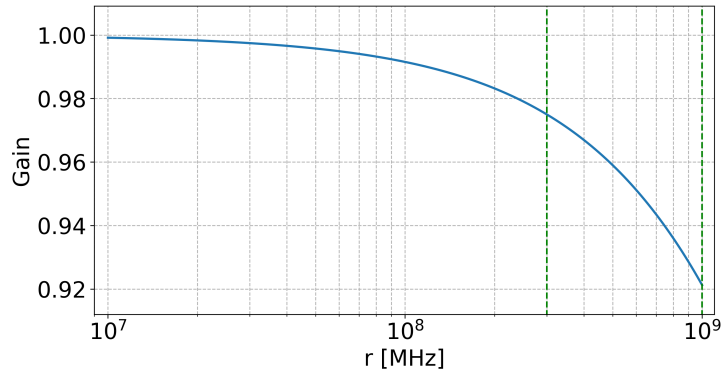


Figure 3: Normalized pixel gain as a function of the hit rate. In case of a hexagonal pixel the expected rate goes from 300 MHz up to 1 GHz corresponding to an effective gain loss ranging from 2.5% to 8%.

The effective gain  $G$  is then computed as a function of the background rate per pixel and reported in Figure 3. Under nominal operating conditions, the camera is expected to see a background rate less than 300 MHz per square cm corresponding to an average gain loss smaller than 2.5%. This is an intrinsic feature of the SiPM which cannot be compensated without changing its internal quenching resistor.

Conversely, the degradation induced by the pile-up on the range available for events observation can be avoided through proper filtering in the sensor interface. Since the sensor time constants differ by three orders of magnitudes, it is possible to filter the undesired tails without significantly affecting the signal of interest. To this end, a high-pass filtering transfer function is achieved with the introduction of AC coupling capacitors throughout the signal processing chain. As shown in Figure 4, the pile-up is successfully removed in the front-end and the entirety of the signal range is available for detection. Moreover, the AC coupling capacitors also provide the design flexibility of defining the bias point of the various stages independently from each other.

*Bandwidth considerations.* The largest portion of the charge generated by the SiPM is delivered through the long tail of the pulse but the fraction which is useful for detection is limited to the initial transient that lasts few nanoseconds and only contains about 1% of the total generated charge; the duration of the fraction of interest introduces a lower bound for the frequencies of interest (around 30 MHz with an hexagonal S13360-3075CS-UVE). The upper

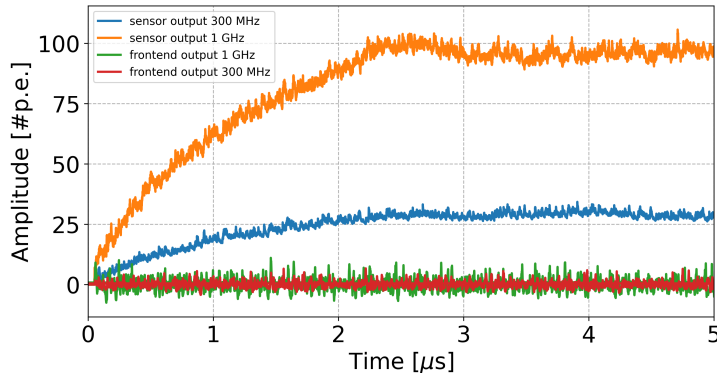


Figure 4: Simulation of the pile-up produced by the Poisson distribution of the background for the pixel hit rates of 300 MHz and 1 GHz. The amplitude is normalized to the pulse amplitude corresponding to a single photo electron, hence the figure shows the potential dynamic range loss caused by the background.

theoretical bound is given by the rising portion of the pulse; in principle a rise time of 200 ps would result in an upper frequency bound of 1.75 GHz, however this value would lead to excessive current consumption and noise within the front-end. Reducing the band of interest to more practical values allows to optimize the SNR by low-pass filtering both the signal and the noise. The effect of the low pass filter on the signal is to introduce a delay (few ns), increase the rising time (from 200 ps to 1 ns) and attenuate the peak amplitude. The effect of the high-pass filter is to remove the pedestal of the slow time constant leading to a shorter pulse at the cost of some undershoot. The output pulse characteristic is reported in Table 2. As shown in Figure 8, the single-ended channel shows a pass-band of (3 MHz, 280 MHz) whereas the differential one has a pass-band of (9 MHz, 520 MHz (can we see it in the measurements?)); the high-pass attenuation is 60 dB/decade due to three AC coupling stages whereas the low-pass attenuation is due to the poles of the amplification stages.

### 3.1. Input stage

The input stage works in voltage mode by amplifying the pulse generated across the external resistor. The preamplifier also needs to provide proper impedance matching over the frequencies of interest as to preserve the pulse shape over the relatively lengthy connection between SiPMs and readout ASIC within the camera (up to tens of cm). The amplifier is built with a

Amplitude [%] relative to peak	Recovery [ns] 1 - 250 pe	Recovery [ns] from saturation
10.00	15	30
1.00	32	65
0.10	95	250
0.01	333	560

Table 2: Output pulse recovery time

common source active stage that employs resistive feedback to define both the bias point and the voltage gain (see Figure 5). The choice of a single ended topology over a differential one provides several design advantages:

- higher bandwidth and phase margin: the lesser quantity of internal nodes minimizes the number of nondominant poles and parasitic capacitances
- power efficiency: the presence of a single circuit branch optimizes the power consumption for a given gain-bandwidth
- higher SNR: due to the smaller number of active components across the signal path the overall contribution to the output noise is reduced
- the asymmetrical current driving capabilities can be exploited for unipolar sensor signals leading to optimal power consumption (not sure it's completely true/verified, check the differential saturated output, acquire both polarities)

A high threshold voltage (HVT) NMOS is chosen as active device to produce a higher dc voltage at the output and, thus, a larger headroom for the negative voltage pulse.

#### 4. Summation stage

The outputs of the four pre-amplifiers are combined by means of an inverting summing amplifier (Figure 5); the output voltages are converted into currents by means of series resistors referenced to the virtual ground of the summing amplifier and added together into the feedback resistor. The summation amplifier is implemented with an NMOS common-source stage;

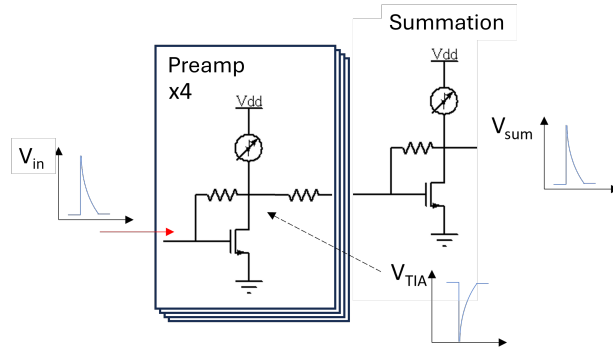


Figure 5: Schematic of the input and summation stages

employing the same topology and active device as the pre-amplifiers allows direct coupling (DC) with the preceding stages. The gain-bandwidth limitation of the summing amplifier introduces a signal attenuation due to current partition at its input node; this attenuation is compensated by the value of the feedback resistor.

## 5. Output buffer

An output buffer is employed to drive the fast voltage pulses towards an external ADC through a matched transmission line. To provide compatibility with different digitization solutions two version have been included in the prototype chip. A single-ended buffer with adjustable DC voltage and a differential buffer; of the eight available pixel channels, four support the differential output and four the single-ended one. Both designs use a two stages configuration and include two adjustable AC coupling capacitors used to implement a passive pulse-shaping filtering. In fact, the decay associated with the slow-time constant needs to be removed to prevent signals pile-up and to minimize the error on the charge acquisition for the following pulses.

### 5.1. Single-ended topology

The single-ended topology is built out of two AC-coupled inverting stages; the first is an NMOS common-source with resistive feedback and adjustable bias current whereas the second is a PMOS common-source with an external resistive load. The single-ended buffer supports a DC coupled  $50 \Omega$  load connected through a matched transmission line. The gain of the second stage is given by the product of the transistor trans-conductance and the

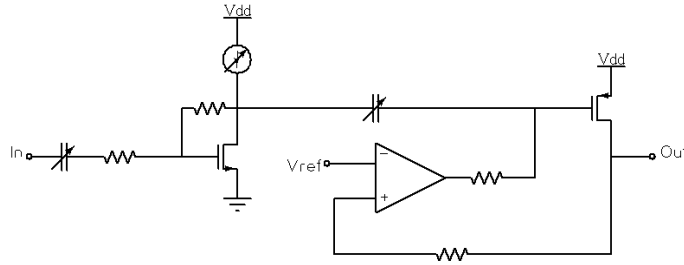


Figure 6: Schematic of the single ended buffer

external load. The second stage includes a low frequency feedback loop that regulates the output voltage by controlling the gate of the amplifying PMOS. This regulation also allows the indirect control of the gain through the bias current of the active device.

### 5.2. Differential topology

The differential topology is made of two stages; a first one that converts the single-ended signal into a pseudo-differential one by means of a succession of two inverting amplifiers and a second stage that buffers the signals towards an AC-coupled differential resistive load ( $100 \Omega$ ). All the stages are implemented with common source amplifiers employing resistive feedback and biased by adjustable current sources.

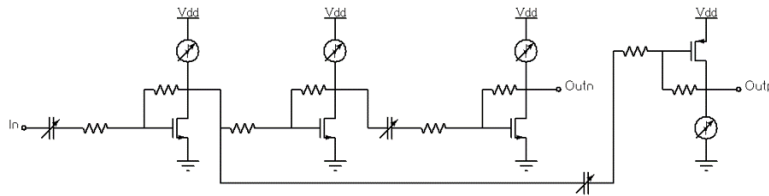


Figure 7: Schematic of the pseudo-differential buffer

## 6. FANSIC configurations

The front-end is AC coupled to the SiPM, in order to allow the voltage biasing of the anode independently from the gate voltage of the TIA. From the application requirements the signal range of interest is defined to go

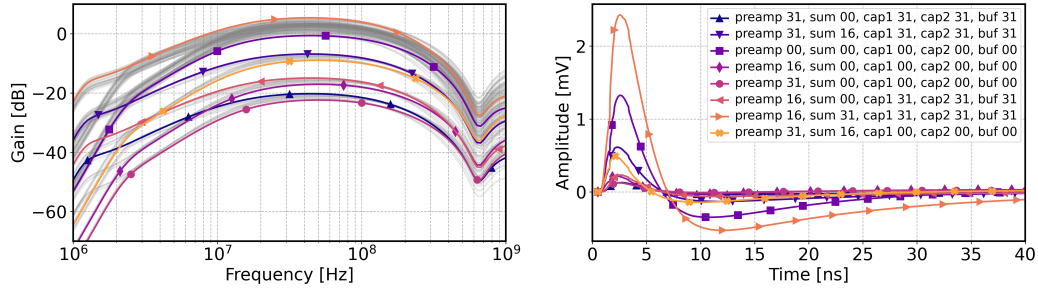


Figure 8: Simulation results of sensor response for various ASIC configurations. The thin gray curves show all the parameter phase space while the colored and thick curves show their extrema.

from 1 to 250 photo-electrons per pixel with a background rate of  $300 \times 10^6$  photons per pixel per second. The AC coupling capacitors placed in between the summation stage and output buffer and in between the two stages of the output buffers can be adjusted independently with two 5-bit words. The effect of these capacitors on the output pulse is to modify the pulse amplitude, width, and amount of undershoot (not independently from each other). The effect of these capacitors on the output pulse is to modify the pulse amplitude, width, and amount of undershoot (not independently from each other). The scan of the entire parameter phase space is shown in Figure 8. One can see that their tuning allows to optimize the response in term of gain, hence dynamic range, speed and SNR.

## 7. Experimental results

### 7.1. Measurement setup

The performance of ASIC is evaluated together with a  $3 \times 3$  mm<sup>2</sup> S13360-3075CS-UVE SiPM from Hamamatsu and a pulsed laser source from Pico-Quant which emits light at a wavelength of 375 nm. The measurement setup is shown in Figure 9: the system under test is placed in a light-tight metal box which also protects the electronics from electromagnetic interference. The actuation of the instrumentation has been completely automatized via Python to obtain a statistically significant sample collection.

### 7.2. FANSIC test PCB

The FANSIC chip has been directly wire-bonded on the test PCB, as shown in Figure 10 (b), to minimize the impact of the parasitic elements. A set of mezzanine boards was developed to accommodate different types



Figure 9: Measurement setup

and shapes of SiPMs or to allow direct connection to an Arbitrary Waveform Generator through micro-coaxial cables. The main components that populate the test PCB are: a manually adjustable LDO in steps of  $25\text{ mV}$  to power the ASIC, a current DAC to provide the required bias currents, a bank of digital level shifters for compatibility with the LVCMOS standard. The board is also equipped with dedicated power connectors to provide the high-voltage bias to the SiPMs and to bypass the LDO and DAC with external sources. An additional FPGA board is used to handle the digital communications between the test board and PC; this General Purpose Inputs Outputs (GPIO) board equips a Cyclone 5 FPGA and allows remote connection through either Ethernet or USB 3.x.

### *7.3. Optical setup calibration*

Since the light source is only adjustable through a manual potentiometer, the intensity delivered on the sensor surface is accurately controlled using a set of optical filters. The neutral density (ND) filters are mounted on an automated rotating wheel (Thorlabs FW212CNEB) and allow to cover over three orders of magnitude of light intensity. The calibration of the optical setup is carried out feeding the light source into an integrating sphere (Thorlabs IS200-4) equipped with a silicon photo-diode and placing a second photo-diode downstream of the filter wheel, at the location intended for the SiPM (as shown in Figure 11). The photo-diodes used are the S1337-1010BQ

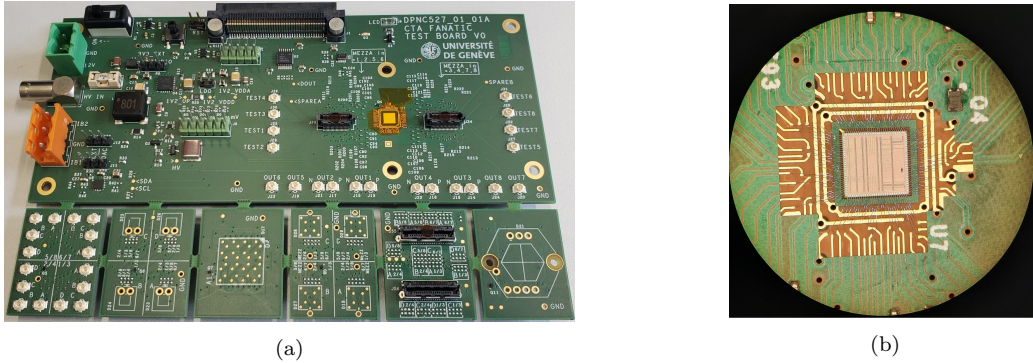


Figure 10: Test PCB (a) with mezzanines to accommodate various SiPM and instrumentation. Detail of the wire-bonded chip (b) with the ground and supply rings around it. Chip dimensions:  $3586 \times 3586 \mu\text{m}^2$ .

from Hamamatsu, the ratio of their output currents is used to characterize the relative filters. The temperature and relative humidity are acquired through the Yocto temperature USB sensor from Yoctopuce. A relative calibration is preferred over an absolute one as the latter needs to account for differences in photo detection efficiency (PDE), area and alignment of the various sensors used. The calibration data is reported in Figure 12.

#### 7.4. ASIC characterization

##### 7.4.1. Output pulse features

The output pulse features are evaluated for low light conditions and with the ASIC configuration which provides a single-photon resolution. The output pulse is shown in Figure 2, the measured waveform is obtained by averaging 10 thousand samples. The light intensity expectation value that is detected by the SiPM corresponds to two photo-electrons. The output pulse shows a peak amplitude gain of  $2.2 \text{ mV/p.e.}$ , a 10% to 90% peaking time of  $1.1 \text{ ns}$ , a full width half maximum (FWHM) of  $2.9 \text{ ns}$  and recovery within 5% of the baseline within  $30.5 \text{ ns}$ . The simulated pulse is also shown in the same figure and an excellent agreement is observed with only  $100 \text{ ps}$  difference in FWHM. The agreement gives great confidence that the sensor characteristics modeled with the Corsi model is accurate and can therefore be used for other sensors whose parameters have been extracted with the same procedure.

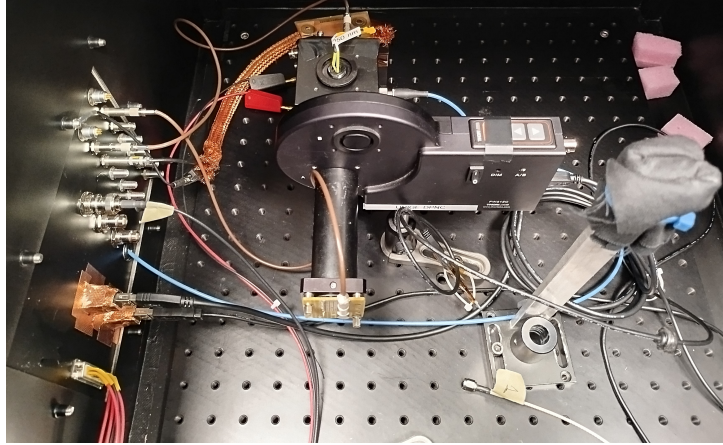


Figure 11: Optical setup for the Neutral Density filters characterization.

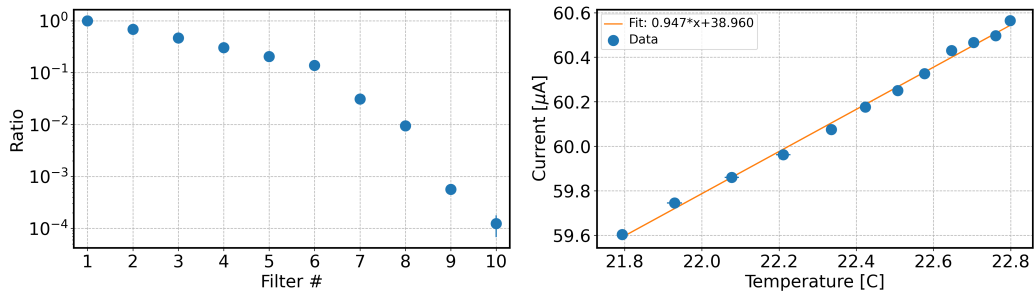


Figure 12: Optical neutral density filters characterization measurements. The left graph shows the relative current measurement of the downstream photo-diode with respect to the lower filter as a function of the filter position. The right side shows, the upstream photo-diode absolute current as a function of the temperature. The coefficients of the linear fit are reported in the legend.

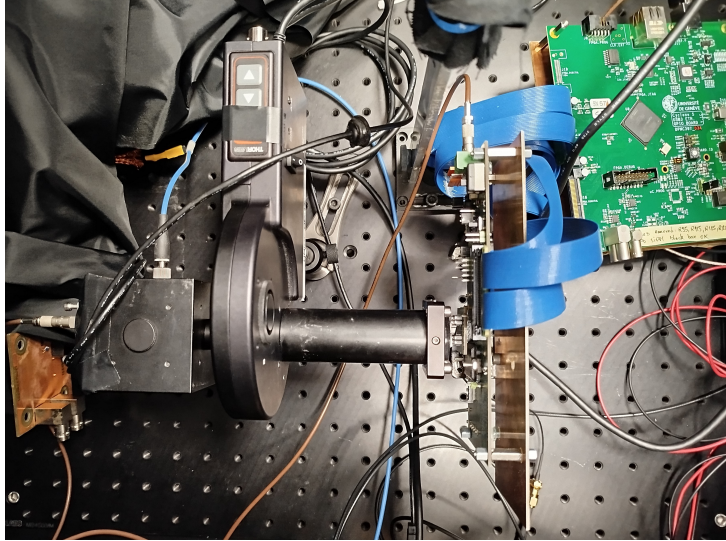


Figure 13: Top view of the optical setup used for the ASIC characterization.

#### 7.4.2. Multi photo-electron response

The multi photo-electron response is evaluated for the single-photon resolution ASIC configuration. The ND filter values are swept to cover the whole dynamic range of the front-end. The laser source intensity is kept fixed to a value that produces few photo-electrons with the higher attenuation settings. The resulting front-end output pulses are shown in Figure 14; the ten waveforms correspond to the lower ND filters including the wheel position with no filter. As the intensity increases, the front-end starts saturating, with the preamplifier being the limiting stage, and the output pulses become longer. When the intensity grows further, the front-end stops reacting because while the preamplifier is completely saturated the SiPM current is sunk by the external resistor. At low and mid intensities, the area under the positive region of the pulses directly correlates with the number of photo-electrons. This correlation is used to derive the transfer characteristic of the front-end by integrating the pulses acquired under the same conditions over a fixed time window of 6 ns and analyzing their statistical distribution.

As visible in Figure 15, on this distribution, the different photo-electron peaks are perfectly distinguishable, up to a count of  $\sim 25$  p.e. As described in [7], this distribution can be fitted with a Generalized Poisson probability density function for which each photo-electron contribution is a Gauss function.

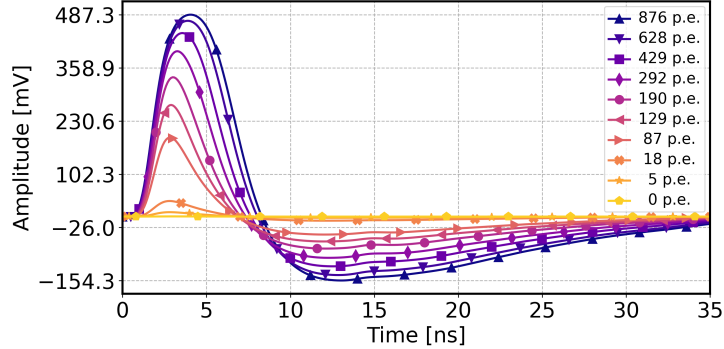


Figure 14: Measured output pulses corresponding to different ND filters. Each waveform is reconstructed by averaging 10 k acquisitions, the estimation of the number of p.e. is based on the ND filter values.

	Gain		$\sigma_e$	$\sigma_s$	$\mu_{XT}$
	a	b			
	[mV.ns]	[mV.ns]	[mV.ns]	[p.e.]	[%]
Value	0.0884	6.8527	0.9604	0.5197	11.9
Fit error	0.0029	0.0400	0.1334	0.0199	0.66

Table 3: Fit result of the MPE shown in Figure 15. The errors are the statistical errors of the fit. The photo-electron gain in the low-mid range is a linear function of the number of photo-electrons, where a and b are the coefficients in the equation:  $Gain = a \cdot N_{pe} + b$ .  $\sigma_e$  represents the electronic noise,  $\sigma_s$  represents the sensor noise,  $\mu_{XT}$  represents the cross talk of the expectation of the number of photo-electrons.

The classical Generalized Poisson parameters include the mean number of detected p.e., the gain of the readout chain, the contribution from the optical cross talk, the statistical noise related to the randomness of the underlying physics of the avalanche in a micro-cell, the electronic noise modeling the contribution of the front-end.

However, as described below in the linearity paragraph, the response of the amplifier is non-linear, which makes this model too simplistic and requires a varying gain as to be consider. In this case, as we only fit distributions below 30 p.e. in mean number of p.e., we assume that the gain is increasing linearly with the number of p.e. The typical fit parameters and their statistical errors are listed in Table 3.

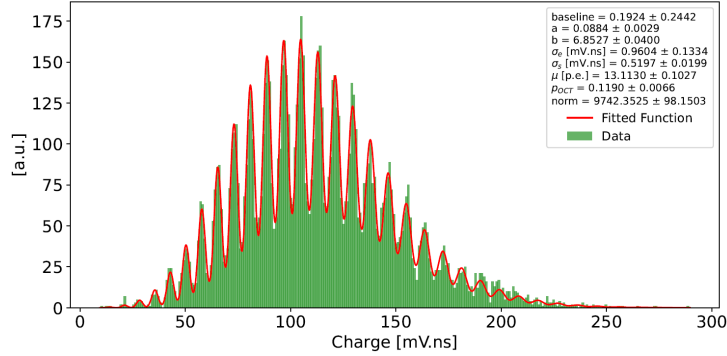


Figure 15: Multi Photo-Electron distribution obtained for one setting light level with the single-ended output. The legend shows the fit parameters with their error.

*Signal to Noise ratio.* The single p.e. signal to noise ratio is computed at low light level as the gain divided by the square root of the noise expressed as in Eq. 5. From the fit we obtain

$$SNR = \frac{Gain}{\sqrt{\sigma_e^2 + \sigma_s^2}} = \frac{6.8527}{\sqrt{0.9604^2 + 0.5197^2}} = 6.27 \quad (5)$$

The SNR estimation from the fit has been confirmed by selecting the waveforms corresponding to a single photo-electron detection and extracting the ratio between the average of the pulse integral and its standard deviation.

*Linearity.* Following the simulation results shown in Figure 16, we expected and observe that in order to fit properly the data, the Generalized Poisson has to be written accounting for a linearly varying gain with parameters  $a$  for the slope and  $b$  the constant. As visible in Table 3, these values differ from the simulation. In all known pSpice simulations of SiPM response published, the gain observed in simulation and measured differs, it is also the case in this work. Both the slope and the offsets are different. It is important to notice in Figure 16 that at around 50 p.e. the gain saturates and even decreases. However, with laboratory measurements, the single photon resolution is lost at these light levels and we therefore cannot measure precisely the location of this transition.

For each intensity setting of the laser source, the ND filters are swept. One of the low intensity dataset is used to compute the expected number of photo-electrons by fitting the charge distribution with a Generalized Poisson probability density function .

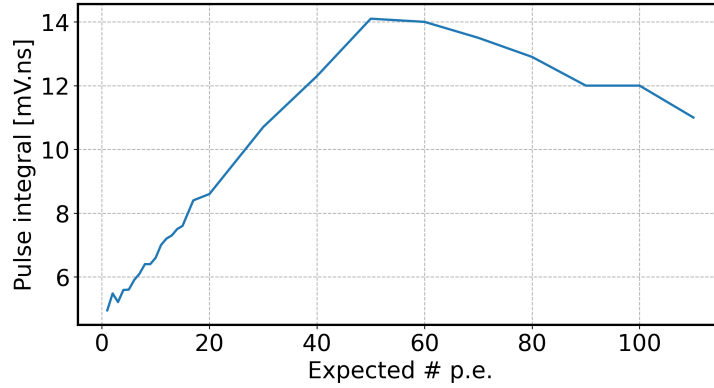


Figure 16: Simulation of the output pulse integral over a time interval of 6 ns as a function of the number of photoelectrons.

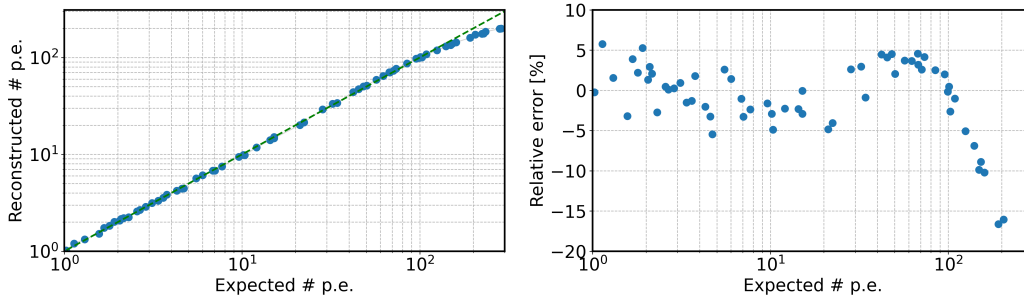


Figure 17: Linearity of the sensor and readout response from 1 to 300 p.e.

The transfer characteristic of the detecting chain is plotted as the reconstructed number of photo-electrons versus the expected number. The latter is computed from the mean of the best fit and adjusted for the attenuation of the selected filter. The reconstructed value is computed as the average of the pulse integral corrected for the cross-talk and divided by the gain extracted from the best fit. The gain deviation from a linear behavior is expected from simulations (see Figure 16) and is caused by the quadratic large-signal gain of single-ended amplifiers such as the common-source topologies employed throughout the signal processing chain.

## 8. Conclusion

In this article an analog front-end for the readout of large silicon photo-multipliers has been presented. The targeted application is for high-speed

cameras of Imaging Atmospheric Cherenkov Telescopes producing images at 1 Gfps with millimeter sized pixels. A prototype ASIC has been developed in standard CMOS 65 nm technology achieving single photon resolution, nanosecond peaking time and 23 mW power consumption per pixel from a 1.2 V supply. The non-linearity is within  $\pm 6\%$  in the range from 1 to 100 photoelectrons.

## 9. Acknowledgment

Supported by the Swiss National Foundation FLARE grant 20FL21 201539.

## References

- [1] H. e. a. Anderhub, Design and operation of FACT - the first G-APD Cherenkov telescope, *Journal of Instrumentation* 8 (2013) 6008P. doi:10.1088/1748-0221/8/06/P06008. arXiv:1304.1710.
- [2] M. Heller, et al., *An innovative silicon photomultiplier digitizing camera for gamma-ray astronomy*, *The European Physical Journal C* 77 (2017) 47. URL: <https://doi.org/10.1140/epjc/s10052-017-4609-z>. doi:10.1140/epjc/s10052-017-4609-z.
- [3] C. Alispach, et al., The SST-1M imaging atmospheric Cherenkov telescope for gamma-ray astrophysics (2024). arXiv:2409.11310.
- [4] T. C. S. Collaboration, The next-generation high-energy discovery machines, 2024. Web Pages .
- [5] M. Heller, et al., The next generation cameras for the Large-Sized Telescopes of the Cherenkov Telescope Array Observatory, *PoS ICRC2023* (2023) 740. doi:10.22323/1.444.0740.
- [6] L. D. MEDINA MIRANDA, Characterization of Photosensitive Devices and Design of an Innovative Large-Sized Gamma-ray Telescope Camera, Ph.D. thesis, University of Geneva, 2023. doi:10.13097/archive-ouverte/unige:167866.
- [7] C. Alispach, et al., Large scale characterization and calibration strategy of a SiPM-based camera for gamma-ray astronomy, *JINST* 15 (2020) P11010. doi:10.1088/1748-0221/15/11/P11010. arXiv:2008.04716.